Monthly Notices
of the
ROYAL ASTRONOMICAL SOCIETY

MNRAS **506,** 2453–2458 (2021)
Advance Access publication 2021 July 2

https://doi.org/10.1093/mnras/stab1863

The near-UV transit of HD 189733b with the *XMM–Newton* optical monitor

George W. King [1,2,3]★ Lía Corrales,[1] Peter J. Wheatley [2,3] Panayotis Lavvas [4] Maria E. Steinrueck [5] Vincent Bourrier,[6] David Ehrenreich,[6] Alain Lecavelier des Etangs[7] and Tom Louden [2,3]

[1]*Department of Astronomy, University of Michigan, Ann Arbor, MI 48109, USA*
[2]*Department of Physics, University of Warwick, Gibbet Hill Road, Coventry CV4 7AL, UK*
[3]*Centre for Exoplanets and Habitability, University of Warwick, Gibbet Hill Road, Coventry CV4 7AL, UK*
[4]*Groupe de Spectrométrie Moléculaire et Atmosphérique, UMR CNRS 7331, Université Reims Champagne Ardenne, 51687 Reims, France*
[5]*Lunar and Planetary Laboratory, University of Arizona, Tucson, AZ 85721, USA*
[6]*Observatoire de l'Université de Genève, 51 chemin des Maillettes, CH-1290 Sauverny, Switzerland*
[7]*Institut d'Astrophysique de Paris, UMR7095 CNRS, Université Pierre & Marie Curie, 98bis boulevard Arago, F-75014 Paris, France*

Accepted 2021 June 25. Received 2021 June 24; in original form 2021 April 28

ABSTRACT

We present analysis of *XMM–Newton* optical monitor observations in the near-ultraviolet of HD 189733, covering 20 primary transits of its hot Jupiter planet. The transit is clearly detected with both the UVW2 and UVM2 filters, and our fits to the data reveal transit depths in agreement with that observed optically. The measured depths correspond to radii of $1.059^{+0.046}_{-0.050}$ and $0.94^{+0.15}_{-0.17}$ times the optically measured radius ($1.187\,R_{\rm J}$ at 4950 Å) in the UVW2 and UVM2 bandpasses, respectively. We also find no statistically significant variation in the transit depth across the 8 yr baseline of the observations. We rule out extended broad-band absorption towards or beyond the Roche lobe at the wavelengths investigated, although observations with higher spectral resolution are required to determine if absorption out to those distances from the planet is present in individual near-UV lines.

Key words: planets and satellites: atmospheres – planets and satellites: individual: HD 189733b – ultraviolet: planetary systems.

1 INTRODUCTION

One of the key aspects in characterizing discovered exoplanets is investigating their atmospheric composition. Transiting planets are particularly good targets for this as the apparent transit depth varies as a function of wavelength. This variation is driven by the bulk elemental composition, molecular, and particulate species present in any atmosphere maintained by the planet. This method of 'transmission spectroscopy' has been widely applied to discover numerous species in the atmospheres of hot Jupiters (e.g. Sing et al. 2016). Attempts to explore much smaller super-Earths (e.g. Kreidberg et al. 2014; Edwards et al. 2020) and even Earth-sized planets (e.g. de Wit et al. 2018) are now being made.

The near-ultraviolet (NUV) is an intriguing wavelength range to target for transmission spectroscopy. There are numerous lines of metallic species that may be observable in absorption (Lothringer et al. 2020), including neutral and singly ionized Fe and Mg. Such absorption can arise from materials in an extended or escaping atmosphere (Fossati et al. 2010; Haswell et al. 2012; Sing et al. 2019; Cubillos et al. 2020). As such, NUV transits could provide insight into mass-loss from exoplanets, complementing observations at other wavelengths such as Ly α (e.g. Vidal-Madjar et al. 2003; Lecavelier des Etangs et al. 2012; Ehrenreich et al. 2015). Additionally, optically measured Rayleigh scattering slopes may extend into the NUV.

The NUV has been largely underexplored. Ground-based measurements can only be made down to about 3000 Å. Furthermore, where observations have been taken, it can be challenging to interpret the results due to the relatively small number of strong, unblended lines, as compared to other wavelengths more commonly used for exoplanet investigations. From space, the *Hubble Space Telescope* (*HST*) is capable of observing in the NUV with its COS, STIS, and WFC3/UVIS instruments (Fossati et al. 2010; Haswell et al. 2012; Vidal-Madjar et al. 2013; Sing et al. 2019; Cubillos et al. 2020; Wakeford et al. 2020), though the majority of transmission spectroscopy experiments performed with *HST* have focused on the optical, near-infrared, and some FUV (e.g. Kreidberg et al. 2014; Ehrenreich et al. 2015; Sing et al. 2016).

In the last few years, both the *XMM–Newton* optical monitor (OM) and *Swift* Ultraviolet/Optical Telescope (UVOT) have been used to detect planetary transits in the NUV. While both facilities are primarily used to make high-energy observations, the 30 cm diameter OM and UVOT observe simultaneously with the various X-ray and gamma-rays telescopes, and both have a range of broad-band filters in the optical and NUV. King et al. (2018) made the first detection of a NUV transit with the OM, using the UVW1 filter to observe a transit of WASP-80b. While consistent with the optically measured transit depth, there was a hint of it being shallower, a result also suggested

★ E-mail: kinggw@umich.edu

Table 1. Adopted stellar and planetary parameters for HD 189733(b).

Parameter	Symbol	Value	Unit	Ref.
Stellar mass	M_*	0.823 ± 0.029	$M_\odot$	1
Stellar radius	R_*	$0.780^{+0.017}_{-0.024}$	$R_\odot$	2
Planet to star radius	R_p/R_*	0.15641 ± 0.00010[a]	–	3
Orbital period	P_{orb}	2.218575200(77)	d	4
Transit centre	T_0	2453955.5255511(88)	BJD_{TDB}	4
Semimajor axis to star radius	a/R_*	8.863 ± 0.020	–	5
Eccentricity	e	0	–	6
Orbital inclination	i	85.710 ± 0.024	°	5

Notes. References: (1) Triaud et al. (2009); (2) Gaia Collaboration (2018); (3) Sing et al. (2011); (4) Baluev et al. (2015); (5) Agol et al. (2010); (6) Bouchy et al. (2005).
[a]As measured at 4950 Å.

by an earlier ground-based *U*-band observation (Turner et al. 2017). The first detection using UVOT was reported for WASP-121b by Salz et al. (2019), with the measured transit depth deeper at the 2σ level than in the optical.

Here, we analyse data taken with the *XMM–Newton* OM across 20 primary transits of the prototypical transiting hot Jupiter HD 189733b, wherein we detect the transit in two different broad-band NUV filters.

1.1 The HD 189733 system

The discovery of HD 189733b was reported by Bouchy et al. (2005), and it remains the closest transiting hot Jupiter to the Earth, orbiting a relatively active K1 dwarf at a distance of just 19.775 ± 0.013 pc (Gaia Collaboration 2018). This fact has led to HD 189733b being one of the most popular targets for both theoretical studies, and follow-up observations to characterize its atmosphere. We give the parameters of the system adopted in this study in Table 1.

At optical wavelengths, the transmission spectrum of HD 189733b shows a steep-gradient slope (e.g. Pont et al. 2008; Sing et al. 2011; Gibson et al. 2012). Excess absorption has been observed at the Na I doublet (e.g. Redfield et al. 2008; Huitson et al. 2012; Louden & Wheatley 2015; Wyttenbach et al. 2015; Khalafinejad et al. 2017), and there is evidence for a K I absorption feature (Pont et al. 2013; Keles et al. 2019, 2020). In the near-infrared, water (Birkby et al. 2013; McCullough et al. 2014; Brogi et al. 2016, 2018) and CO (de Kok et al. 2013; Rodler, Kürster & Barnes 2013; Brogi et al. 2016) have both been detected. The subdued amplitude of both the water and wings of the sodium line features, together with the steep optical slope, point towards the presence of high-altitude aerosols in the atmosphere (Pont et al. 2013; Sing et al. 2016). The planet is also one of an increasing number to have a helium excess measured in the metastable 10 830 Å triplet (Salz et al. 2018; Guilluy et al. 2020).

HD 189733b's atmosphere has also been studied at shorter wavelengths, with Ly α transit observations showing that H I is moving beyond the Roche lobe and escaping the atmosphere (Lecavelier Des Etangs et al. 2010, 2012; Bourrier et al. 2013, 2020). The transit depths at Ly α wavelengths of up to 15 per cent have been observed to be variable (Lecavelier des Etangs et al. 2012). Additionally, Ben-Jaffel & Ballester (2013) measured a 6.4 per cent transit in O I, and there is a time variable absorption signature in the Si III line that could arise from a bow-shock formed ahead of the planet in its orbit (Bourrier et al. 2013, 2020). In X-rays, Poppenhaeger, Schmitt & Wolk (2013) presented evidence of the X-ray transit possibly being as deep as 8 per cent. Our analysis of the simultaneously taken X-ray data will be published separately (Wheatley et al., in preparation; King et al., in preparation). Taken together, these observations show that the X-ray and extreme-ultraviolet (together, XUV) heating of HD 189733b has led to its atmosphere being extended, and in at least the case of H I, escaping. As is thought to be the case for almost all hot Jupiters (e.g. Owen & Jackson 2012; Bourrier & Lecavelier des Etangs 2013), the rate of escape of material becoming unbound to the planet is not high enough to significantly change the planet's structure.

2 OBSERVATIONS AND DATA REDUCTION

XMM–Newton has observed HD 189733b on 25 separate occasions from 2007 through 2015, with 20 of these covering a primary transit. In Table 2, we present details of these 20 transit observations (the PI in each case was P. Wheatley).

Our analysis here focuses on the data taken with the OM, a 30 cm aperture telescope with a photon-counting instrument at Cassegrain focus, operating in the visual and NUV (Mason et al. 2001). The observations presented in the work exploited the rare ultraviolet capabilities of the OM, using the UVW1, UVW2, and UVM2 filters.[1] All 20 of these observations were taken in imaging mode, along with a single, small fast mode window to capture the light from HD 189733 at 11 ms resolution.

As per their definition in Table 2, observations 1 and 2 employed the UVM2 (effective wavelength = 2910 Å; width[2] = 830 Å) and UVW1 (2310 Å; 480 Å) filters, respectively, while the other 18 all used the UVW2 (2120 Å; 500 Å) filter. The observation 2 data were rendered unusable by the brightness of the source resulting in excessive coincidence losses that could not be corrected. We do not analyse or discuss this observation any further. The UVM2 filter choice for observation 1 lead to a count rate of $9.4\,s^{-1}$, and the 18 observations that employed the UVW2 filter had an average count rate of $4.9\,s^{-1}$.

We reduced the data using the standard software OMICHAIN and OMFCHAIN within the Scientific Analysis System, for the image and fast mode data, respectively. Although the fast mode data is captured at 11 ms resolution, in practice, the standard reduction pipeline produces a time series file at 10 s resolution by default, a setting which we do not alter. Following the running of the chains, we corrected each observation's photometric data using the procedure as described in King et al. (2018), wherein we correct the fast mode time series using the image mode data.

3 DATA ANALYSIS AND RESULTS

3.1 UVW2 observations

The bulk of our analysis efforts focused on the 18 observations taken with the UVW2 filter. We restrict our analysis to the phases where there are data for at least 16 of the 18 observations: 0.9142–1.0508. Visual inspection of the binned, phase-folded light curve, shown in Fig. 1 revealed a clear transit detection at the expected time, according

[1]For more information about the filters of the OM, see the *XMM–Newton* Users Handbook: http://xmm-tools.cosmos.esa.int/external/xmm_user_support/documentation/uhb/omfilters.html
[2]The width of a filter with a constant transmission equal to that at the effective wavelength, and which has the same effective area as the real OM filter in question.

Table 2. Table detailing the 20 *XMM–Newton* observations of HD 189733 analysed in this paper.

No.	ObsID	Start time (BJD_{TDB})	End time (BJD_{TDB})	Start – Stop Phase	Exp. time (ks)	Filter
1	0506070201	2007-04-17T14:16	2007-04-18T04:36	0.8431 – 1.1121	44.0	UVM2
2	0692290201	2013-05-09T20:26	2013-05-10T07:02	0.8965 – 1.0958	33.5	UVW1
3	0692290301	2013-11-03T08:21	2013-11-03T17:42	0.9015 – 1.0768	30.7	UVW2
4	0692290401	2013-11-21T01:26	2013-11-21T12:38	0.8847 – 1.0950	37.4	UVW2
5	0744980201	2014-04-05T05:33	2014-04-05T17:24	0.8118 – 1.0346	39.8	UVW2
6	0744980301	2014-05-02T01:50	2014-05-02T07:40	0.9120 – 1.0217	18.8	UVW2
7	0744980401	2014-05-13T02:23	2014-05-13T12:31	0.8804 – 1.0709	31.8	UVW2
8	0744980501	2014-05-15T10:24	2014-05-15T18:49	0.9327 – 1.0908	25.6	UVW2
9	0744980601	2014-05-17T14:48	2014-05-17T23:13	0.9168 – 1.0749	27.4	UVW2
10	0744980801	2014-10-17T16:36	2014-10-18T02:24	0.9136 – 1.0978	28.8	UVW2
11	0744980901	2014-10-19T21:06	2014-10-20T06:11	0.8996 – 1.0702	28.0	UVW2
12	0744981001	2014-10-22T02:06	2014-10-22T12:43	0.8952 – 1.0945	33.5	UVW2
13	0744981101	2014-10-24T06:43	2014-10-24T17:05	0.8833 – 1.0779	32.6	UVW2
14	0744981301	2014-11-08T20:44	2014-11-09T05:52	0.9075 – 1.0792	28.2	UVW2
15	0744981201	2014-11-11T01:05	2014-11-11T12:50	0.8907 – 1.1114	39.4	UVW2
16	0744981401	2014-11-13T07:13	2014-11-13T15:08	0.9075 – 1.0562	25.6	UVW2
17	0744980701	2014-11-15T10:15	2014-11-15T20:07	0.8660 – 1.0512	30.8	UVW2
18	0744981501	2015-04-13T03:05	2015-04-13T14:13	0.8914 – 1.1006	35.4	UVW2
19	0744981601	2015-04-17T13:02	2015-04-17T22:57	0.8814 – 1.0677	31.0	UVW2
20	0744981701	2015-04-19T19:34	2015-04-20T05:39	0.9054 – 1.0948	31.6	UVW2

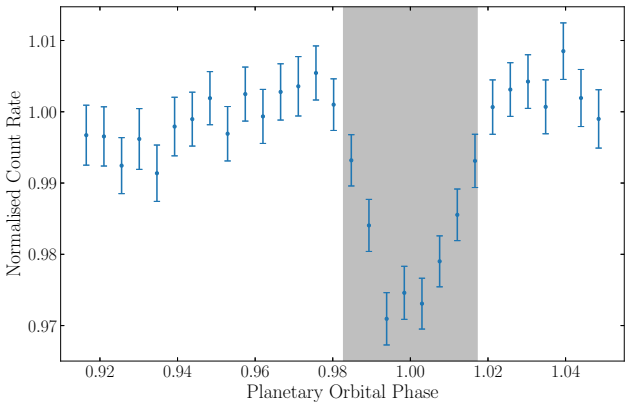

Figure 1. Binned, phase folded OM light curve for the 18 observations with UVW2. No correction has been made in this figure for out-of-transit trends. The shaded region is the full duration of the optical transit, with the phases plotted according to the ephemeris in Table 1.

to the optical ephemeris. The light curve, however, shows structure in the out-of-transit data. By examining the individual observation light curves, we saw that this out-of-transit trend varied in shape from observation to observation.

We performed several MCMC fits to the time series data, binned to the reduction pipeline standard cadence of 10 s, and with each observation normalised to its out-of-transit count rate. We used the BATMAN (Kreidberg 2015) transit model with a quadratic limb darkening law, with Gaussian priors applied to the coefficients $u_1 = 0.0594 \pm 0.0200$ and $u_2 = 0.0160 \pm 0.0200$. These coefficients were determined by passing values of the effective area of the UVW2 filter as a function of wavelength through the TABULATEDFILTER function of Limb Darkening Toolkit (Parviainen & Aigrain 2015). Gaussian priors were also placed on the system's inclination, i, and ratio of the semimajor axis and stellar radius, a/R_*, according to their values and uncertainties listed in Table 1.

We accounted for the out-of-transit trends by multiplying the transit model by a quadratic, $a_j t^2 + b_j t + c_j$, allowing the coefficients to vary across the different observations, j. However, in order to help constrain the coefficients and avoid them going off to erroneous values, we initially performed a fit using a single quadratic that was the same for each observation, yielding $a = -0.997^{+0.697}_{-0.676}$, $b = 2.02^{+1.33}_{-1.37}$, and $c = -0.016^{+0.676}_{-0.654}$. In our final fits, we placed uniform priors on the quadratic coefficients for each observation, forcing them to be within 2σ of this initial single quadratic fit. Additionally, at this same step, we ran a second, similar fit in which the only difference was that we allowed the mid-transit time t_0 to vary, in order to verify there was no offset in this value from the ephemeris present in the data. The best-fitting t_0 was consistent to within 1σ of the optical ephemeris (in phase, $t_0 = 1.00057^{+0.00081}_{-0.00082}$). In all of our following analyses, we accordingly fixed t_0 according to the optically measured ephemeris.

Our three final fits investigated the measured planet radius in the UVW2 band ($R_{p,UVW2}$). In the first of these, we allowed $R_{p,UVW2}/R_*$ to change between all of the observations, applying a wide uniform prior, $0 < \frac{R_{p,UVW2}}{R_*} < 1$, to prevent unphysical values. As we were interested in the relative changes of $R_{p,UVW2}$ across each observation, in this fit we fixed the values of i, a/R_*, u_1, and u_2, as opposed to utilising the Gaussian priors. In Fig. 2, we plot the measured $R_{p,UVW2}/R_*$ as a function of observation number. This plot shows that the individual UVW2 transit depths are consistent with each other, and with the transit depths observed in the optical (see Table 1). The mean and median of these 18 measurements are $R_{p,UVW2}/R_* = 0.1555 \pm 0.0071$ and 0.159, respectively. In terms of $R_{p,UVW2}/R_{p,opt}$, where $R_{p,opt}$ is the optically measured radius (at 4950 Å), these values are 0.994 ± 0.045 and 1.00. We statistically tested for variation of $R_{p,UVW2}/R_*$ by comparing against a constant model equal to the mean of the 18 values, 0.15722. This gave $\chi^2_{red} = 0.71$ and a p-value of 0.79, indicating that the values are consistent with being constant within the uncertainties.

In the second fit, we further investigated variation in the transit on longer time-scales, by forcing $R_{p,UVW2}/R_*$ to be the same for each observation within (but not between) the following defined epochs: 'Autumn 2013' (Observations 3 and 4 in Table 2), 'Spring 2014' (Observations 5 to 9), 'Autumn 2014' (Observations 10–17), and

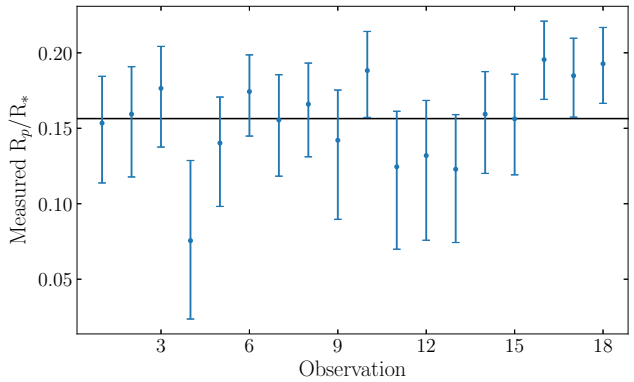

Figure 2. Measured value of the ratio of the planet and stellar radius, $R_{p,UVW2}/R_*$, in each transit observation with the UVW2 filter on the optical monitor. The solid horizontal line depicts the measured value of R_p/R_* at optical wavelengths.

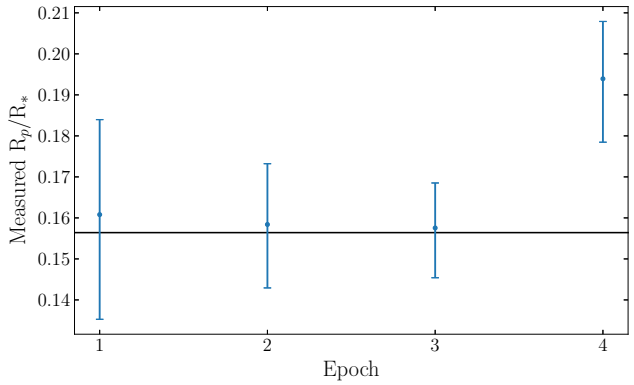

Figure 3. Measured value of the ratio of the planet and stellar radius, $R_{p,UVW2}/R_*$, at each of the four defined epochs (see main text). The solid horizontal line depicts the measured value of R_p/R_* at optical wavelengths.

'Spring 2015' (Observations 18–20). The same wide uniform prior as before was used for each of the four $R_{p,UVW2}/R_*$ values, while i, a/R_*, u_1, and u_2 were again fixed for this fit. In Fig. 3, we plot the measured $R_{p,UVW2}/R_*$ for each of these four epochs. Although the final epoch for the Spring 2015 data shows a hint of a larger $R_{p,UVW2}/R_*$ compared to the other three epochs, the four points are consistent with a constant model equal to the mean, with $\chi^2_{red} = 1.47$ and a p-value of 0.22.

Following these findings, we ran an MCMC wherein we forced $R_{p,UVW2}/R_*$ to be the same across all 18 transits. The Gaussian priors on i, a/R_*, u_1, and u_2 were restored. In Fig. 4, we plot the phase-folded light curve with the best-fitting model from this MCMC plotted over the top. In this plot, the best-fitting out-of-transit trends have been removed from each observation's light curve before phase folding and binning. Parameter details for this MCMC run are given in Table 3. Most notably, this run gives a best-fitting value of $R_{p,UVW2} = 1.059^{+0.046}_{-0.050} R_{opt}$, a value that is consistent with the optical radius of the planet to just outside 1σ.

3.2 UVM2 observation

The observation on 2007 April 17/18 (observation 1 in Table 2) was taken using the UVM2 filter. The resulting light curve, displayed in Fig. 5, showed evidence of a transit dip at the expected phase. We ran an MCMC fit to the time series data binned to 10 s. We

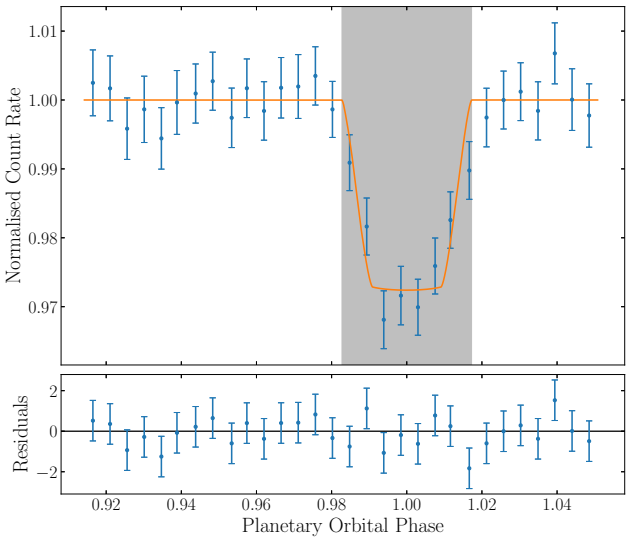

Figure 4. Top panel: binned, phase folded OM light curve for the 18 UVW2 observations, with the best-fitting out-of-transit quadratic trends removed. Plotted in orange is the best-fitting model, where $R_{p,UVW2}$ was forced to be constant across all 18 light curves. Bottom panel: residuals of the model.

Table 3. Parameters used for and obtained from the final, best MCMC run for each OM filter's observations. In the case of UWV2, this is the fit where $R_{p,UVW2}/R_*$ was forced to be the same across all observations.

Parameter	Value		Unit
	UVW2	UVM2	
	Gaussian priors		
u_1	0.0594 ± 0.0200	0.0618 ± 0.0250	
u_2	0.0160 ± 0.0200	0.0204 ± 0.0250	
a/R_*	8.863 ± 0.020		
i	85.710 ± 0.024		°
	Fixed Value		
t_0	1.0		phase
	Free, fitted parameter		
R_p/R_*	$0.1657^{+0.0072}_{-0.0078}$	$0.146^{+0.023}_{-0.026}$	
	Derived parameter		
R_p	$1.059^{+0.046}_{-0.050} R_{opt}$	$0.94^{+0.15}_{-0.17}$	R_{opt}

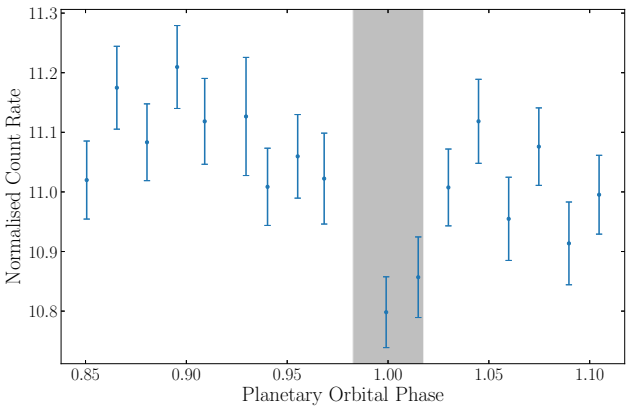

Figure 5. Binned OM UVM2 light curve for observation 1. This time series has not been corrected for out-of-transit trends.

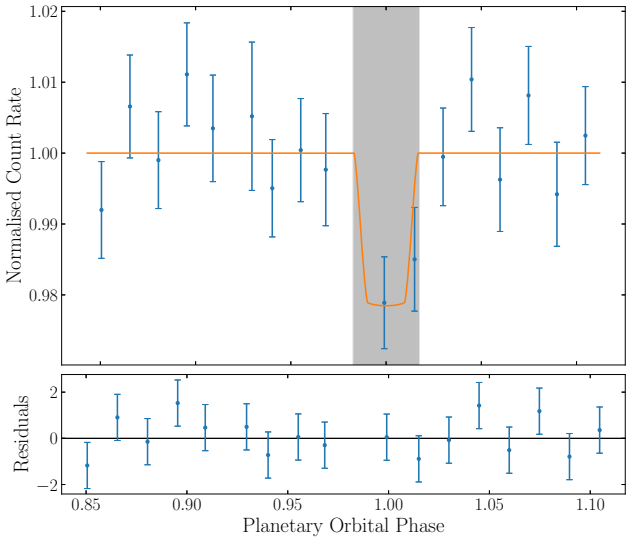

Figure 6. As Fig. 4, but for the single UVM2 light curve and associated fit.

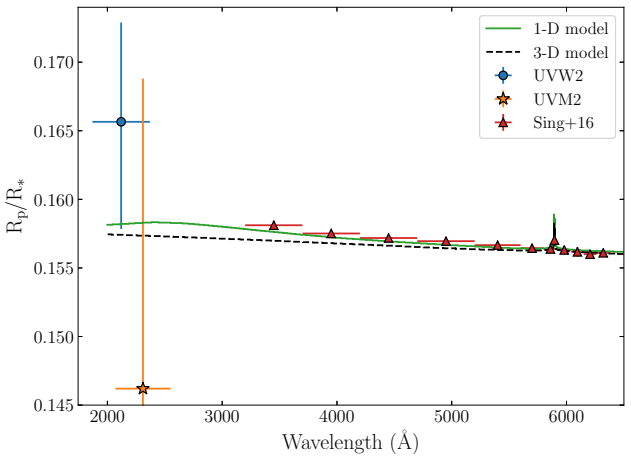

Figure 7. Transmission spectrum of HD 189733b in the optical and NUV. The points associated with the transit measurements presented in this work are given with the blue circle (UVW2 filter) and the orange star (UVM2). The red triangles are the data presented in Sing et al. (2016; only that blueward of 6500 Å is displayed) – the error bars on those points are too small to be seen on this scale. The green solid line is that expected by the 1D model extended from the work of Lavvas & Arfaux (2021), and the black-dashed line is that expected by the 3D model extended from the work of Steinrueck et al. (2020). The Roche lobe of the planet ($3\,R_{\rm opt}$, or $R_{\rm p}/R_* = 0.471$) is too far off the scale of the plot to be visible.

used a similar procedure to that outlined for the UVW2 data, with the same priors on $R_{\rm p,UVM2}/R_*$, i, a/R_*. The out-of-transit trend was again accounted for by multiplying the transit model by a quadratic in time. We derived limb darkening coefficients for the UVM2 filter using Limb Darkening Toolkit of $u_1 = 0.0618 \pm 0.0250$ and $u_2 = 0.0204 \pm 0.0250$, again using these values to place a Gaussian prior on the fit coefficients.

The light curve and the best fitting model from the MCMC are plotted in Fig. 6, with the best fitting out-of-transit quadratic having been removed from the light curve. Parameter details for this MCMC run are again given in Table 3. Our best-fitting value for the radius of the planet in this observation is $R_{\rm p,UVW2} = 0.94^{+0.15}_{-0.17}\,R_{\rm opt}$, and so consistent with the optically measured radius.

4 DISCUSSION

The transmission spectrum of HD 189733b exhibits a steep optical slope that may arise from either the presence of atmospheric aerosols or contamination from star-spots (Pont et al. 2008, 2013; Sing et al. 2011; McCullough et al. 2014). In Fig. 7, we plot a transmission spectrum of HD 189733b. In addition to the two broad-band filter measurements presented here, we include optical data bluewards of 6500 Å (Pont et al. 2013; McCullough et al. 2014; Sing et al. 2016). The single observation UVM2 point is not particularly informative as to whether the steep slope continues into the UV, given the large size of the error bar. One thing to note is that detailed simulations of aerosol formation in hot Jupiter atmospheres predict that transmission spectrum will eventually flatten at shorter wavelengths (Powell et al. 2019). Both the UVM2 and UVW2 data points are consistent with that scenario, although the error bars are also too large to concretely prove or rule out enhanced absorption from other sources, such as Fe II and Mg II (Turner et al. 2016; Salz et al. 2019; Lothringer et al. 2020).

The measurements unquestionably rule out average opaque region sizes across these bandpasses similar to or exceeding the size of the Roche lobe ($3\,R_{\rm opt}$). Opaque region sizes measured at other wavelengths (e.g. Ly α: Lecavelier des Etangs et al. 2012; Bourrier et al. 2020) have indicated there are detectable levels of escape of atmospheric material beyond this point. This and other such signals are typically observed in specific lines of interest and not in broad-band measurements such as those presented here.

For comparison, in addition to the NUV and optical measurements, in Fig. 7 we also plot two recent transit spectra derived from simulations of the HD 189733b atmosphere, extended to 2000 Å. The 1D model from Lavvas & Arfaux (2021) includes disequilibrium chemistry and radiative feedback from photochemical hazes, which dominate the NUV opacity of the upper atmosphere, 0.1 mbar and above. They found that hazes also work to heat the upper atmosphere above 1 mbar, which increases the effective scale height at short wavelengths. Utilising soot opacities, their model (the green curve in Fig. 7) provides a good fit to the steep transmission curve for wavelengths less than 6000 Å. The 3D model from Steinrueck et al. (2020) features a GCM derived HD 189733b transmission spectrum that includes the effects of a non-homogeneous distribution of photochemical hazes at the terminator. Assuming a uniform particle size of 3 nm and utilizing soot opacities, they find that enhancing the vertical mixing in the GCM (the black-dashed curve in Fig. 7) is required to approach the steep slope observed at short wavelengths, but their 3D model fits the observed transmission spectrum at wavelengths longer than 6000 Å better than the 1D models.

The UVW2 measurement across 18 transits hints at a continuation of the steep blue slope into the NUV. However the uncertainties on our measurement mean that a flattening out of this feature, as seen in the 1D model (see Fig. 7) cannot be ruled out. We can, however, decisively rule out the average transmission region size across the UVW2 bandpass being similar in size to the Roche lobe, which is interesting in the context of previous studies of the neutral and singularly ionized Fe and Mg lines a few hundred Angstroms either side of 2500 Å. Transits in these lines have previously been used to detect these species in the exospheres of exoplanets (Fossati et al. 2010; Sing et al. 2019; Cubillos et al. 2020). However, we cannot determine without higher resolution observations or further modelling whether there is no detectable exosphere Fe and Mg at

these wavelengths, or if the broadness of the bandpasses used in this work have sufficiently washed out the deeper transits expected in those narrow lines.

5 CONCLUSIONS

We have observed the near-UV transit of prototypical hot Jupiter HD 189733b in three broad-band filters across 20 observations taken with the *XMM–Newton* OM. We successfully detected transits in two of these filters, UVW2 (18 observations) and UVM2 (1 observation), with the star proving too bright in the single UVW1 observation and saturating the camera. HD 189733b is the third planet to have a near-UV transit detection by *XMM–Newton* or *Swift*.

With MCMC fits to the data using BATMAN transit light curve models, we measured transit depths for UVW2 and UVM2 that are statistically consistent with the optically measured radius of the planet. We also show that there is no significant variation in $R_{p,UVW2}/R_*$ across the 18 observations taken with UVW2 filter, within the measured uncertainties. The same conclusion was also reached when considering variation in $R_{p,UVW2}/R_*$ between four defined epochs in Section 3.1.

Comparing with previous transmission spectra measurements taken with *HST*, our measurement allows for either a continuation of the steep slope observed at optical wavelengths or a flattening off of this slope in the near-UV. Our results emphatically rule out the broad-band transmission region size extending out close to or beyond the planet's Roche lobe, however, such signals could still be possible in narrow wavelength regions around lines such of neutral and singly ionized Fe and Mg. Higher resolution observations are required to investigate the transit signal in those lines.

ACKNOWLEDGEMENTS

PJW acknowledges support by STFC under consolidated grants ST/P000495/1 and ST/T000406/1. DE has received funding from the European Research Council (ERC) under the European Union's Horizon 2020 research and innovation programme (project FOUR ACES; grant agreement No 724427). VB has received funding from the European Research Council (ERC) under the European Union's Horizon 2020 research and innovation programme (project SPICE DUNE; grant agreement No 947634). This project has also been carried out in the frame of the National Centre for Competence in Research PlanetS supported by the Swiss National Science Foundation.

DATA AVAILABILITY

The *XMM–Newton* data used in this work are publically available from the *XMM–Newton* Science Archive: http://nxsa.esac.esa.int/nxsa-web/#search

REFERENCES

Agol E., Cowan N. B., Knutson H. A., Deming D., Steffen J. H., Henry G. W., Charbonneau D., 2010, ApJ, 721, 1861
Baluev R. V. et al., 2015, MNRAS, 450, 3101
Ben-Jaffel L., Ballester G. E., 2013, A&A, 553, A52
Birkby J. L., de Kok R. J., Brogi M., de Mooij E. J. W., Schwarz H., Albrecht S., Snellen I. A. G., 2013, MNRAS, 436, L35
Bouchy F. et al., 2005, A&A, 444, L15
Bourrier V., Lecavelier des Etangs A., 2013, A&A, 557, A124
Bourrier V. et al., 2013, A&A, 551, A63
Bourrier V. et al., 2020, MNRAS, 493, 559
Brogi M., de Kok R. J., Albrecht S., Snellen I. A. G., Birkby J. L., Schwarz H., 2016, ApJ, 817, 106
Brogi M., Giacobbe P., Guilluy G., de Kok R. J., Sozzetti A., Mancini L., Bonomo A. S., 2018, A&A, 615, A16
Cubillos P. E., Fossati L., Koskinen T., Young M. E., Salz M., France K., Sreejith A. G., Haswell C. A., 2020, AJ, 159, 111
de Kok R. J., Brogi M., Snellen I. A. G., Birkby J., Albrecht S., de Mooij E. J. W., 2013, A&A, 554, A82
de Wit J. et al., 2018, Nat. Astron., 2, 214
Edwards B. et al., 2021, AJ, 161, 44
Ehrenreich D. et al., 2015, Nature, 522, 459
Fossati L. et al., 2010, ApJ, 714, L222
Gaia Collaboration, 2018, A&A, 616, A1
Gibson N. P. et al., 2012, MNRAS, 422, 753
Guilluy G. et al., 2020, A&A, 639, A49
Haswell C. A. et al., 2012, ApJ, 760, 79
Huitson C. M., Sing D. K., Vidal-Madjar A., Ballester G. E., Lecavelier des Etangs A., Désert J. M., Pont F., 2012, MNRAS, 422, 2477
Keles E. et al., 2019, MNRAS, 489, L37
Keles E. et al., 2020, MNRAS, 498, 1023
Khalafinejad S. et al., 2017, A&A, 598, A131
King G. W. et al., 2018, MNRAS, 478, 1193
Kreidberg L., 2015, PASP, 127, 1161
Kreidberg L. et al., 2014, Nature, 505, 69
Lavvas P., Arfaux A., 2021, MNRAS, 502, 5643
Lecavelier Des Etangs A. et al., 2010, A&A, 514, A72
Lecavelier des Etangs A. et al., 2012, A&A, 543, L4
Lothringer J. D., Fu G., Sing D. K., Barman T. S., 2020, ApJ, 898, L14
Louden T., Wheatley P. J., 2015, ApJ, 814, L24
Mason K. O. et al., 2001, A&A, 365, L36
McCullough P. R., Crouzet N., Deming D., Madhusudhan N., 2014, ApJ, 791, 55
Owen J. E., Jackson A. P., 2012, MNRAS, 425, 2931
Parviainen H., Aigrain S., 2015, MNRAS, 453, 3821
Pont F., Knutson H., Gilliland R. L., Moutou C., Charbonneau D., 2008, MNRAS, 385, 109
Pont F., Sing D. K., Gibson N. P., Aigrain S., Henry G., Husnoo N., 2013, MNRAS, 432, 2917
Poppenhaeger K., Schmitt J. H. M. M., Wolk S. J., 2013, ApJ, 773, 62
Powell D., Louden T., Kreidberg L., Zhang X., Gao P., Parmentier V., 2019, ApJ, 887, 170
Redfield S., Endl M., Cochran W. D., Koesterke L., 2008, ApJ, 673, L87
Rodler F., Kürster M., Barnes J. R., 2013, MNRAS, 432, 1980
Salz M. et al., 2018, A&A, 620, A97
Salz M., Schneider P. C., Fossati L., Czesla S., France K., Schmitt J. H. M. M., 2019, A&A, 623, A57
Sing D. K. et al., 2011, MNRAS, 416, 1443
Sing D. K. et al., 2016, Nature, 529, 59
Sing D. K. et al., 2019, AJ, 158, 91
Steinrueck M. E., Showman A. P., Lavvas P., Koskinen T., Tan X., Zhang X., 2021, MNRAS, 504, 2
Triaud A. H. M. J. et al., 2009, A&A, 506, 377
Turner J. D., Christie D., Arras P., Johnson R. E., Schmidt C., 2016, MNRAS, 458, 3880
Turner J. D. et al., 2017, MNRAS, 472, 3871
Vidal-Madjar A., Lecavelier des Etangs A., Désert J. M., Ballester G. E., Ferlet R., Hébrard G., Mayor M., 2003, Nature, 422, 143
Vidal-Madjar A. et al., 2013, A&A, 560, A54
Wakeford H. R. et al., 2020, AJ, 159, 204
Wyttenbach A., Ehrenreich D., Lovis C., Udry S., Pepe F., 2015, A&A, 577, A62

This paper has been typeset from a TEX/LATEX file prepared by the author.